Exp Fluids (2014) 55:1829
DOI 10.1007/s00348-014-1829-y

RESEARCH ARTICLE

The impact of twine/mesh ratio on the flow dynamics through a porous cylinder

B. Levy · H. Friedrich · J. E. Cater · R. J. Clarke · J. P. Denier

Received: 13 April 2014 / Revised: 27 July 2014 / Accepted: 24 September 2014

Abstract The impact of the twine/mesh ratio on the flow through a porous hollow cylinder of diameter D has been experimentally investigated at Reynolds number $Re = 800$ with a surface porosity varying from 0.67 to 0.90. Our porous cylinder models are inspired by aquaculture pens in that they have similar geometries, and porosities, to those nets commonly used within the aquaculture industry. We show that the surface porosity alone is not the key parameter determining the flow topology of the model, but rather a non-dimensional parameter $\alpha = t^{0.5} D^{0.5}/m$ (based upon twine thickness t, mesh void m and cylinder diameter D) effectively collapses first-order moments. Three different wake regimes are observed in the flow for different twine/mesh ratios: a laminar flow regime where streamlines pass through the model without significant deformation; a partially occluded flow, where the mean flow is decelerated, and a flow with a fully developed recirculation zone exhibiting a von Kármán vortex street similar to that produced in the wake of a solid cylinder. Our observation that the flow structure depends upon the parameter α, rather than simply the surface porosity, is supported by calculated dispersion times of virtual particles released both inside the model and within the wake. The particle distributions display three distinct dispersion behaviours, from nearly linear to a logarithmic decay slower than that of a solid cylinder, thus emphasising the existence of multiple flow regimes and the importance of the relative twine/mesh ratio.

B. Levy · J. E. Cater · R. J. Clarke · J. P. Denier (✉)
Department of Engineering Science, University of Auckland, Auckland, New Zealand
e-mail: j.denier@auckland.ac.nz

H. Friedrich
Department of Civil and Environmental Engineering, University of Auckland, Auckland, New Zealand

1 Introduction

In 2010, the United Nations identified the intensive aquaculture industry as the fastest growing food industry in the world (FAO 2010). With more than 45 % of the world's seafood consumption already produced in farms, this growth is expected to continue (Subasinghe et al. 2009; FAO 2010). However, this flourishing industry is facing difficulties. Pens, also called *gravity cages* or *net cages*, have to withstand extreme weather conditions. In storms, the wave power reaches destructive levels for aquaculture infrastructure, as experienced in 2013 in the Philippines during 'super-typhoon' Yolanda. Moreover, protected river delta production does not guarantee success, as experienced by Vietnamese producers in the Red River Delta, where floods, storms and sea tides frequently inflict significant losses (Stickney 2009). There is an increasing trend to locate aquaculture fish cages offshore, and work has been undertaken to accurately model the deformation of the pen under loading by ocean or tidal currents (Lader and Enerhaug 2005; Zhao et al. 2007; Moe et al. 2010; Kristiansen and Faltinsen 2012; Zhao et al. 2013). This industry is also challenged by environmental concerns, such as biowaste dispersion (Venayagamoorthy et al. 2011), parasite growth (Salama and Murray 2011; Torrissen et al. 2013) and sea floor deterioration below the farms (Buryniuk et al. 2006; Halwart et al. 2007). Further fundamental research on the biology, environmental impact, solid mechanics and fluid dynamics of pens is consequently needed, a conclusion reached by Klebert et al. (2013) in their recent review on aquaculture hydrodynamics.

It is not yet possible to easily investigate the detailed flow through pens at full-scale or at field-equivalent Reynolds numbers, as they range in magnitude up to $O(10^7)$. However, at laboratory scale, optical techniques are more easily applied. At model scale, the number and size of the elements in a full net is difficult to manufacture and dynamic scaling of the structural response is difficult. Compromises are therefore required, thus explaining why past experimental studies have had a Reynolds number ranging from 10^3 to 10^5. Computational studies are further complicated by the fact that the flow physics at in-field Reynolds numbers is poorly understood and so results from CFD calculations are often, at best, compromised by crude parameterisations of flow physics. Here, we present results of an experimental programme that focuses on the net-like structure of pens commonly used in the aquaculture industry. We do this by studying the flow through a hollow, but otherwise rigid, cylinder of aspect ratio 1.375 for various surface porosities. Our focus is upon porosity which matches that expected of aquaculture pens, modelled at much smaller dimensions. The twine thickness and the mesh void together define the surface porosity (Fig. 1).

The flow past a solid cylinder at Reynolds numbers less than a thousand is a classical fluid dynamical problem which has been extensively considered in the literature (Williamson and Roshko 1988; Williamson 1996; Norberg 2003). Multiple flow regimes have been identified, ranging from steady flow to three-dimensional unsteady flow. The von Kármán vortex street is the most well-known signature of the flow in this Reynolds number range. A fixed solid cylinder at $Re = 800$ displays a 2S mode, which is characterised by contra-rotating vortices alternatively shed in the wake of the cylinder (Williamson and Roshko 1988). Modifications made to the structure by adding geometrical artieacts, holes or porosity create changes in the wake dynamics and the resulting turbulent stresses (Zdravkovich 1981; Baek and Karniadakis 2009; Levy and Liu 2013).

Recent studies using porous cylinders surrounding a solid core Ozkan et al. (2013); Mandal et al. (2013) have used grids to create the porosity. The porous layer is used for control purposes, either for wake vortex dynamics or for altering the boundary layer. Porous cylinders, or porous bluff bodies, are also used in aerodynamic applications for blowing/suction manipulation of the boundary layer (Fransson et al. 2004; Arcas and Redekopp 2004; Dong et al. 2008; Feng and Wang 2012; Camarri et al. 2013). Suction is known to reduce the growth of viscous Tollmien-Schlichting waves within the boundary layer, thus delaying transition to turbulence and consequently reducing drag around the body; blowing increases the azimuthal velocity which can lead to vortex breakdown if a sufficient amount of energy is added and the Swirl number exceeds $\sqrt{2}$ (Billant et al. 1998). The opposite behaviour has been observed for flows at supercritical Reynolds numbers, where a slight blowing can decrease the back flow and stabilise the wake (Delaunay and Kaiktsis 2001). A study of the fluid motion through a porous cylinder in the laminar steady regime ($Re \leq 40$), motivated by applications in the bio-chemistry industry, demonstrated that the separation point location was dependent upon cylinders permeability (Bhattacharyya et al. 2006).

There are multiple studies on flow past porous obstructions made of a group of cylinders (Ball et al. 1996; Takemura and Tanaka 2007; Nicolle and Eames 2011; Zong and Nepf 2011). Whether it is experimental or computational, on a circular arrangement or a square one, at Reynolds numbers ranging from 400 to 35,000, the tendency is always the same: as the porosity is increased, the vortex shedding appears further downstream of the cylinder up to a limit at which the shedding of the overall structure is no longer observed. At this point, every single element of the obstruction creates an identifiable wake. Three different flow regimes have been observed for porosity ranges from $\epsilon \geq 0.94$, $0.94 \geq \epsilon \geq 0.85$ and $0.85 \geq \epsilon$.

The present study has a similar approach but instead of varying the porosity of the obstruction, only the surface porosity is modified. Hence, we investigate the flow around and through a hollow cylindrical structure with varying surface porosity, resulting in different levels of base bleed flow (Wood 1967), and how the surface porosity impacts upon the flow dynamics.

2 Experimental apparatus

Experimental data were acquired using a recirculating flume with a measured turbulence intensity of less than 3 %. The flume cross-sectional area is 0.4 m × 0.4 m, length 4 m and was operated at a flow rate of 0.02 m/s. The models were manufactured using 3D printing technology, capable of a spatial resolution of 20 µm. This method guarantees precision and regularity of the twines (t) and the mesh, (m), (Fig. 1). The resulting surface porosity, defined as

$$\epsilon = \mathscr{S}_{\text{mesh}} / \mathscr{S}_{\text{cylinder}}$$

with $\mathscr{S}_{\text{mesh}}$ the surface area of the mesh and $\mathscr{S}_{\text{cylinder}}$ the surface area of the cylinder, varies from $\epsilon = 0.67$ to 0.90; the mesh void is square. Each model has a constant diameter $D = 40$ mm and height $h = 55$ mm and is attached to a lid of height 6.5 mm. Two vertical ribs of 1 mm thickness have been added inside all models to insure rigidity of the most fragile models (Fig. 1). The model is

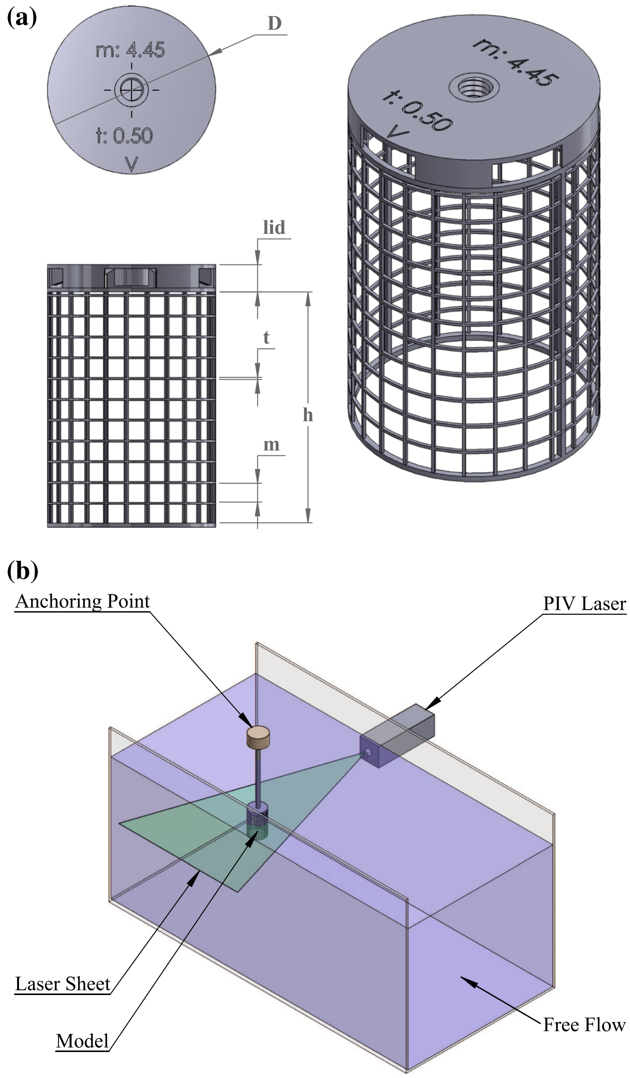

Fig. 1 Schematic of the model and its position within the flume. Shown are **a** the dimensions of the model, indicating twine thickness t, mesh void m, outside diameter of the model D and height of the model h and **b** the setup of a model in the flume and the PIV laser sheet

Table 1 Models mesh void (m), twine thicknesses (t), surface porosity, ϵ, and scaling parameter α

Case	Mesh (mm)	Twine (mm)	ϵ	$\alpha = t^{0.5}D^{0.5}/m$
Solid	N.A.	N.A.	0	N.A.
1	8.89	0.50	0.90	0.50
2	6.67	0.50	0.87	0.67
3	4.45	0.50	0.81	1.00
4	2.22	0.50	0.67	2.47
5	4.45	0.25	0.90	0.71
6	4.45	0.75	0.73	1.23
7	4.45	1.00	0.67	1.42
8	2.22	0.25	0.81	1.42
9	6.67	0.75	0.81	0.82
10	6.67	1.00	0.76	0.95
11	8.89	0.75	0.85	0.62
12	8.89	1.00	0.81	0.71

placed at the centre of the flume to ensure the symmetry of the upstream flow. A list of the twine and mesh dimensions used is shown in Table 1. The effect of a small rotation of the cylinder mount was investigated, especially in regard to the ribs. A rotation of 10° has a negligible impact on the flow. Only a reduction $\leq 7\ \%$ of the time-averaged velocity magnitude localised at $y/D \in [-0.35; -0.58]$ could be measured. The lid was designed so as to not influence the flow at mid-height of the model; furthermore, the ribs, being positioned towards the inside of the model, have a negligible impact on the flow.

Dye flow visualisation was used to reveal flow patterns in the wake and investigate the existence of the three flow regimes described by Gansel et al. (2012), Klebert et al. (2013). Time-resolved particle image velocimetry (TR-PIV) was conducted. For PIV data acquisition, a laser sheet was generated perpendicular to the model axis, at $y = h/2$ (shown in Fig. 1). The flow Reynolds number is $Re = 800$, based on the model diameter D, the upstream free flow U_{inf}. The PIV system consists of a 5W CW Nd: YVO4 laser from Spectra-Physics Millenia installed beside the flume, and a Basler A504k 120 fps camera mounted with Nikkor 20 mm, Nikkor 50 mm or Tokina 100 mm lenses placed below the flume. The frequency of acquisition used for the experiments was 40 or 50 fps for acquisition times of 125 or 240 s, resulting in 2,500 and 6,000 image pairs, respectively. The velocity flow field was obtained by cross-correlating 50 % overlapping windows of 32 × 32 pixels or 16 × 16 pixels, yielding fields of up to 160 × 128 vectors, with a spatial resolution of 3.438 mm (0.086 D), 1.973 mm (0.0493 D) or 0.768 mm (0.0192 D) respectively. Inside the models, the velocity field was obtained by cross-correlating 75 % overlapping windows of 64 × 64 pixels. This setting allows processing of the areas of shadow made by the twines, where particles are sometimes not detectable.

To visualise dispersion patterns, we used two-dimensional particle tracking based on the instantaneous velocity field obtained from PIV data (Sheard et al. 2007). For this purpose, virtual particles are introduced at each PIV correlation node at $t = 0$ and are displaced according to the value of the velocity field, measured for the time step Δt. Once the new position of each particle is calculated, the velocity vector at $t + \Delta t$ imposes the new displacement of the particles. This provides a visualisation of the instantaneous flow, which is presented in Sect. 3.2.

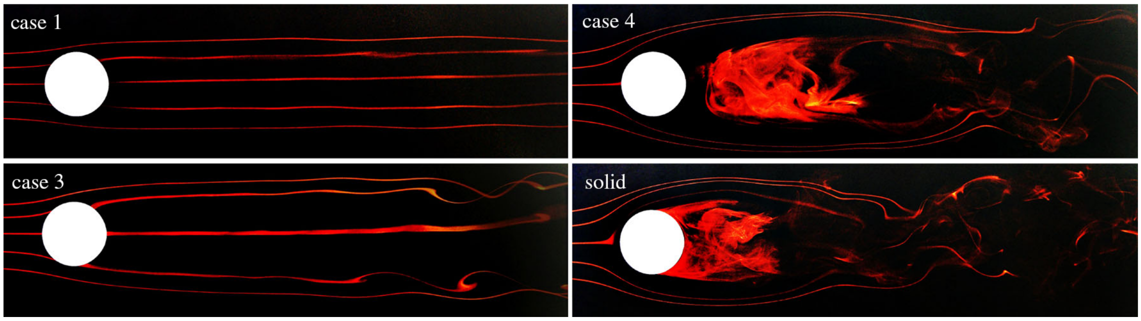

Fig. 2 Dye visualisation of the instantaneous flow around three models displaying different flow regimes compared with a solid cylinder at $Re = 800$. Shown are cases 1, 3, 4 and, for reference, the solid cylinder. The twine and mesh dimensions are defined in Table 1

3 Results

Dye visualisations (Fig. 3) show the distinct flows that develop with changes in the model geometry. The existence of three different wake regimes for such a geometry is confirmed: (1) a completely penetrating flow in which the streamlines pass through the model without any visible deformation (Case 1, Fig. 2), (2) a partially penetrating flow where part of the flow is decelerated, thus allowing the development of a Kelvin-Helmholz instability in the extended far-wake (Case 3, Fig. 2), and (3) a flow with a fully developed recirculation zone exhibiting a von Kármán vortex street (Case 4 Fig. 2) similar to that observed behind a solid cylinder (Solid, Fig. 2). This result is in agreement with previous studies on similar geometries (Zong and Nepf 2011; Gansel et al. 2012). We now present data from PIV measurements in order to quantify the three observed flow cases.

3.1 Time-averaged flow

The impact of the twine/mesh ratio on the wake, at a distance of up to $10D$ downstream, was initially studied using the PIV data acquired with a 20-mm focal-length lens. The time-averaged vorticity contours shown in Fig. 3 show that the wake structures differs significantly, depending on the twine/mesh ratio. At a non-dimensional vorticity magnitude of $\omega D/U_{\mathrm{inf}} \geq 0.2$, the apparent wake length extends from $6D$ to over $10D$. By comparison, the apparent wake behind the solid cylinder at the same Reynolds number is approximately $4D$. At a constant mesh void size, an increase in twine thickness leads to an increase in the magnitude of the maximum vorticity (Fig. 3, left) and a decrease in the bleed flow. Conversely, for a constant twine thickness, increasing the mesh void yields a greater bleed flow and therefore a lower maximum vorticity (Fig. 3, right). The vorticity magnitude outside the model increases with a decrease in the surface porosity as it leads to a faster flow circumventing the model. However, our results demonstrate that the surface porosity is not the only controlling parameter, since for Cases 4 and 7, which have an identical porosity of $\epsilon = 0.67$, the time-averaged wake is not identical (Fig. 3). Case 4 exhibits a wake which is 14 % shorter, but has a 6 % higher maximum vorticity magnitude than Case 7.

Cases 1 and 5 also present equivalent surface porosities, despite having different twine thicknesses and mesh voids. However, the bleed flow velocity differs significantly; for Case 1, it is 50 % greater than Case 5 which demonstrates that for the geometry investigated, the porosity is not the unique parameter defining the bleed flow. Also, Case 5 has an apparent wake which is 12 % wider and has a 50 % higher maximum vorticity magnitude than Case 1 (Fig. 3).

The time-averaged velocity magnitude was extracted from the same set of PIV data at two different cross sections, $x/D = 1$, Fig. 4a, and $y/D = 0$, Fig. 4d. Each model exhibits a distinct wake. Again, it is observed that the porosity is not the sole parameter that determines the time-averaged behaviour of the wake. At one diameter downstream, Cases 4, 7 and Cases 1, 5, as pairs with the same porosity, show different bleed flow, differing by over 400 and 50 %, respectively.

The model wake is clearly dependent on the twine/mesh ratio, and the ability of the porosity alone to collapse the data proved unlikely. Indeed, no power of ϵ was found to collapse the flow velocity data (the best "agreement" using porosity alone is shown in Fig. 4b, e, using ϵ^{-1}). A more appropriate empirical non-dimensional parameter for collapsing the data has been found to be $\alpha = t^{0.5}D^{0.5}/m$. To verify the robustness of this parameter, five further models were added to the investigation, namely Cases 8–12 (Table 1). Cases 9–12 display behaviour characterising the first or second flow regime, whereas Case 8 displays behaviour corresponding to the third flow regime.

Figure 4 shows plots of velocity profiles and velocity decay. Figure 4c, f shows the velocity profiles and decay collapsed with the parameter α. The parameter α adequately collapses the data for the models presenting the

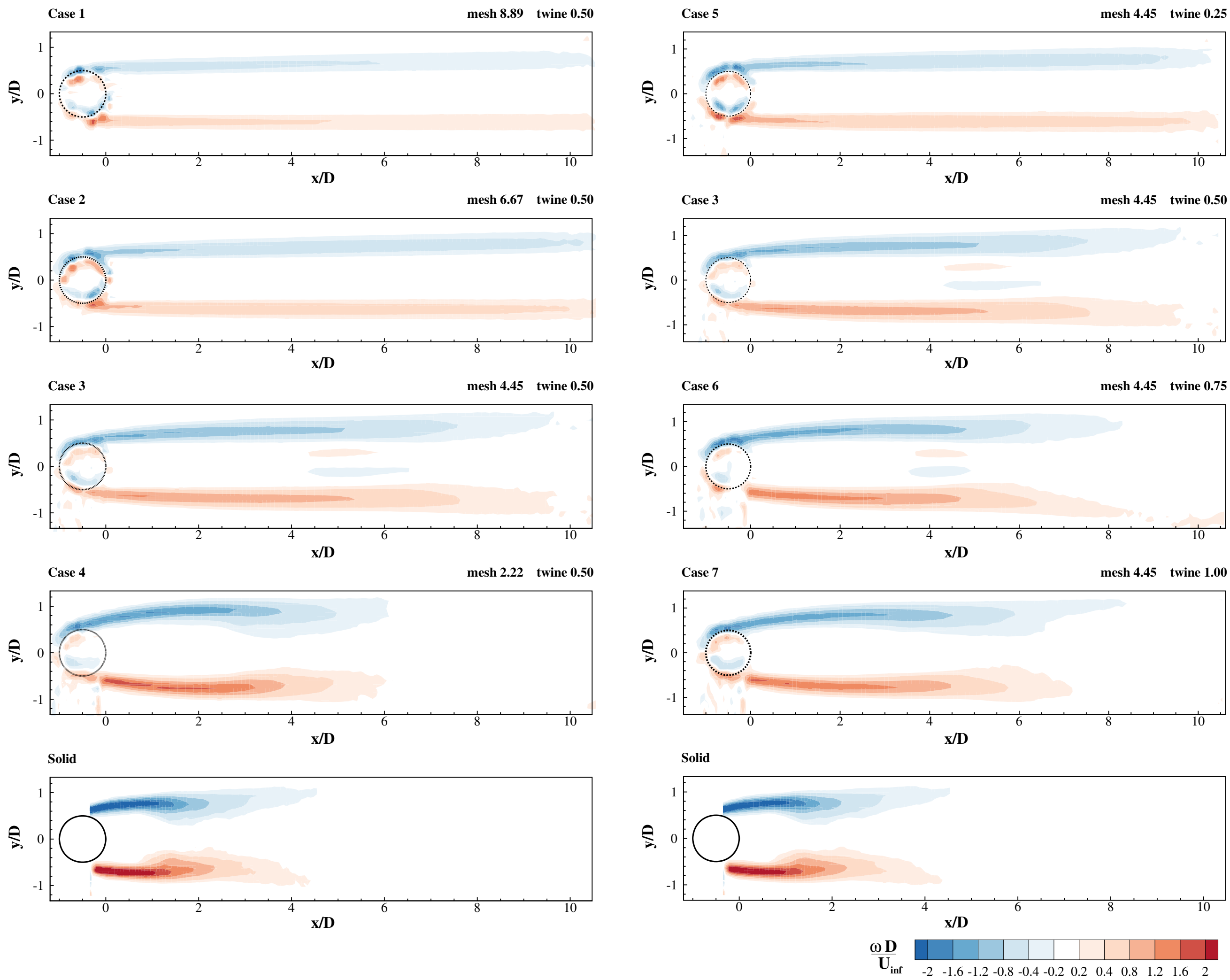

Fig. 3 Time-averaged vorticity topology: constant twine, varying mesh (*left*); constant mesh, varying twine (*right*)

first and second flow regime, with a porosity ϵ greater than 0.67. However, this collapse is not satisfactory for those flows in the third flow regime, Cases 4 and 7 and arguably Case 8. The flow dynamics change significantly with the third regime, as the shedding becomes the predominant mechanism in defining the wake structure. Case 7 shows a transitional flow pattern, corresponding to a change from, or to, the third regime.

A closer look at the flow inside the models in the near wake ($x/D < 0.5$), using PIV with the 100-mm focal-length lens, further emphasises the flow differences between each case (Fig. 5). The trend observed in the wake, suggesting that the flow is not solely determined by the porosity ϵ, is also supported by these measurements. Positive and negative vorticity is generated by each twine. We also note that the local Reynolds number, based on the twine thickness, is $Re_t = 21$. Inside the model, we observe parallel wakes generated by the separated flow past a bluff body at low Reynolds number, akin to the one observed past a cylinder at $Re \leq 49$ (Coutanceau and Bouard 1977; Williamson 1996), for all Cases presented in Fig. 5, with the exception of Case 4. For Case 4, the flow inside the cylinder presents a different topology. There is no steady symmetrical wake past every twine, but instead two areas of opposite vorticity on each "side" of the model (above and below the y-axis in Fig. 5) where the flow is reoriented by nearly 90°. Cases 1 and 5, which have an equivalent porosity ϵ = 0.90, show distinct differences in the time-averaged vorticity. For Case 1, the flow inside the model is faster and the vorticity magnitude greater (up to 82 % at the centre of the model) than experienced in Case 5.

The wake of a bluff body, in the presence of a constant upstream velocity, depends upon its shape and size. If we consider Cases 1 to 4, we observe that at a constant twine thickness, the distribution and magnitude of vorticity inside the model decreases as the mesh void is reduced. Along the

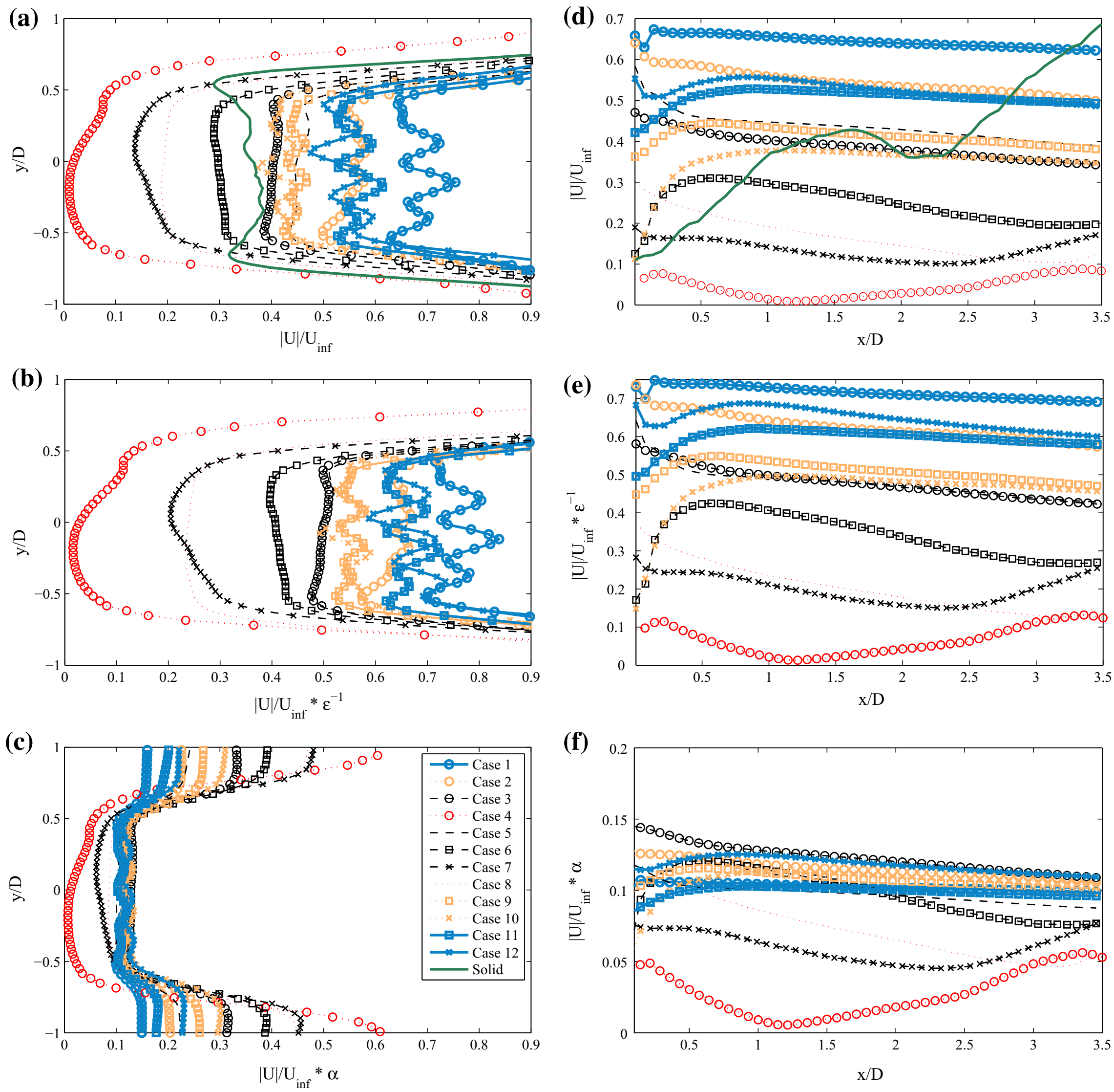

Fig. 4 **a** Velocity profiles in the wake of 13 different models at $x/D = 1$ or one diameter from the downstream side of the models; **b** velocity profiles collapsed using ϵ; **c** velocity profiles collapsed using $\alpha = t^{0.5}D^{0.5}/m$; **d** velocity decay in the wake of 13 different models at $y/D = 0$; **e** velocity decay collapsed using ϵ; **f** velocity decay collapsed using α

centerline of the model, the vorticity is reduced by up to 28, 82 and nearly 100 %, as the mesh void is reduced by 25, 50 and 75 %, respectively. The same cannot be said for the influence of the twine thickness. At a constant mesh, the modification of the twine thickness from 0.25 to 1.00 does not influence the vorticity magnitude inside the model, except near the uppermost and lowermost portions of the model (Fig. 5, Cases 5, 3, 6 and 7). However, the flow velocity inside the model shows an increase as a result of the reduction in the twine thickness, which in turn corresponds to an increase in the surface porosity ϵ. A similar behaviour occurs when the twine is kept constant and the mesh void is increased. It therefore appears that the mesh void is the key parameter regulating the vorticity magnitude inside the model. We now investigate the impact of variations in this parameter is investigated using particle tracking.

3.2 Instantaneous flow particle tracking

Figure 7 shows the motion of virtual particles, introduced into the wake region of the flow. The particle paths are calculated for each time steps, imposed by the acquisition frequency of the TR-PIV data, using the TR-PIV velocity fields (Sheard et al. 2007). The particle tracking visualisations show the displacement of particles behind the models. In doing so, they highlight the increased

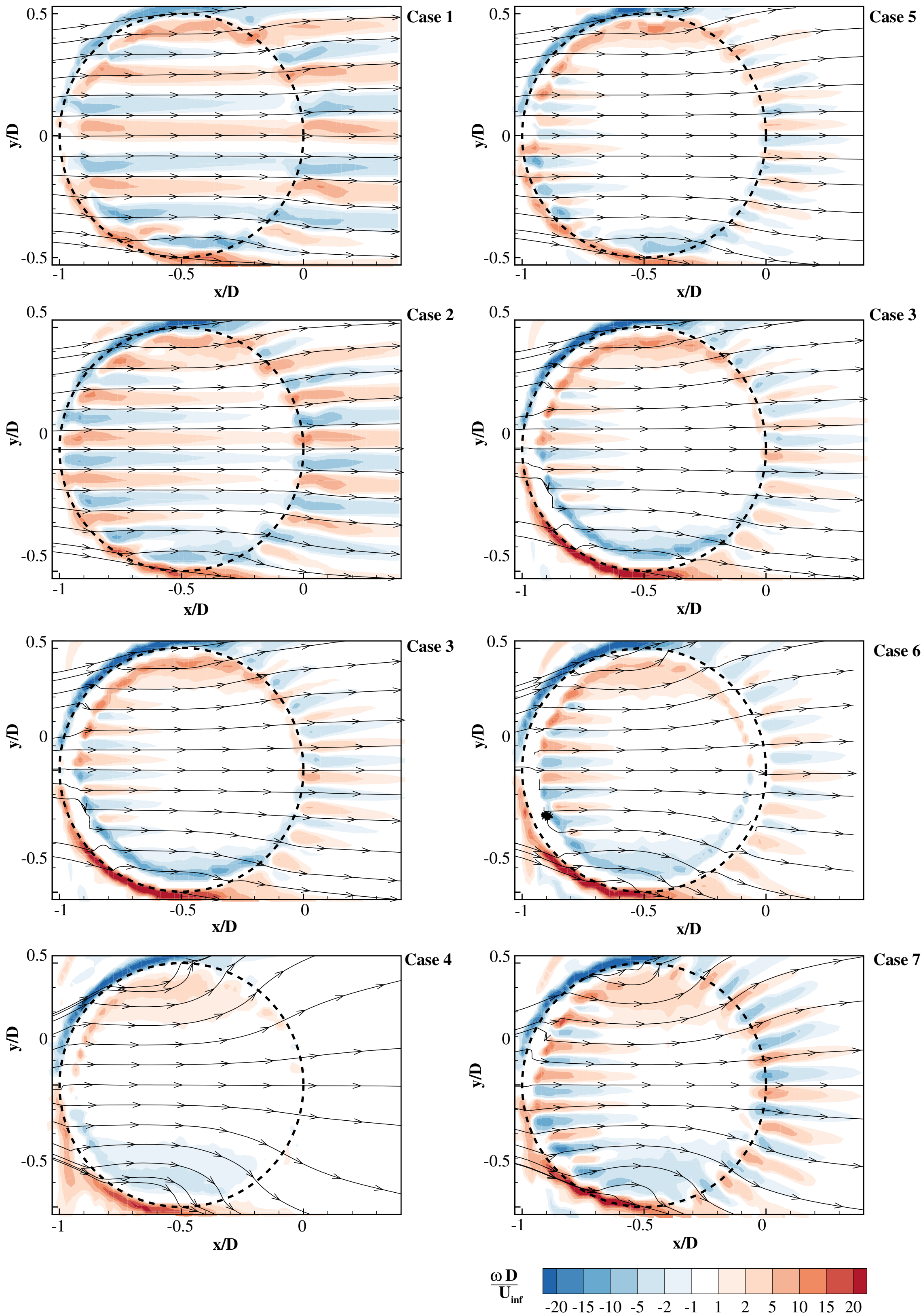

Fig. 5 Time-averaged vorticity contours and streamlines. Shown are results for constant twine, varying mesh (*left*) and constant mesh, varying twine (*right*). The 13 streamlines are equally dispersed along the central *y*-axis of the model at $x = 0$, emphasising the flow velocity variations

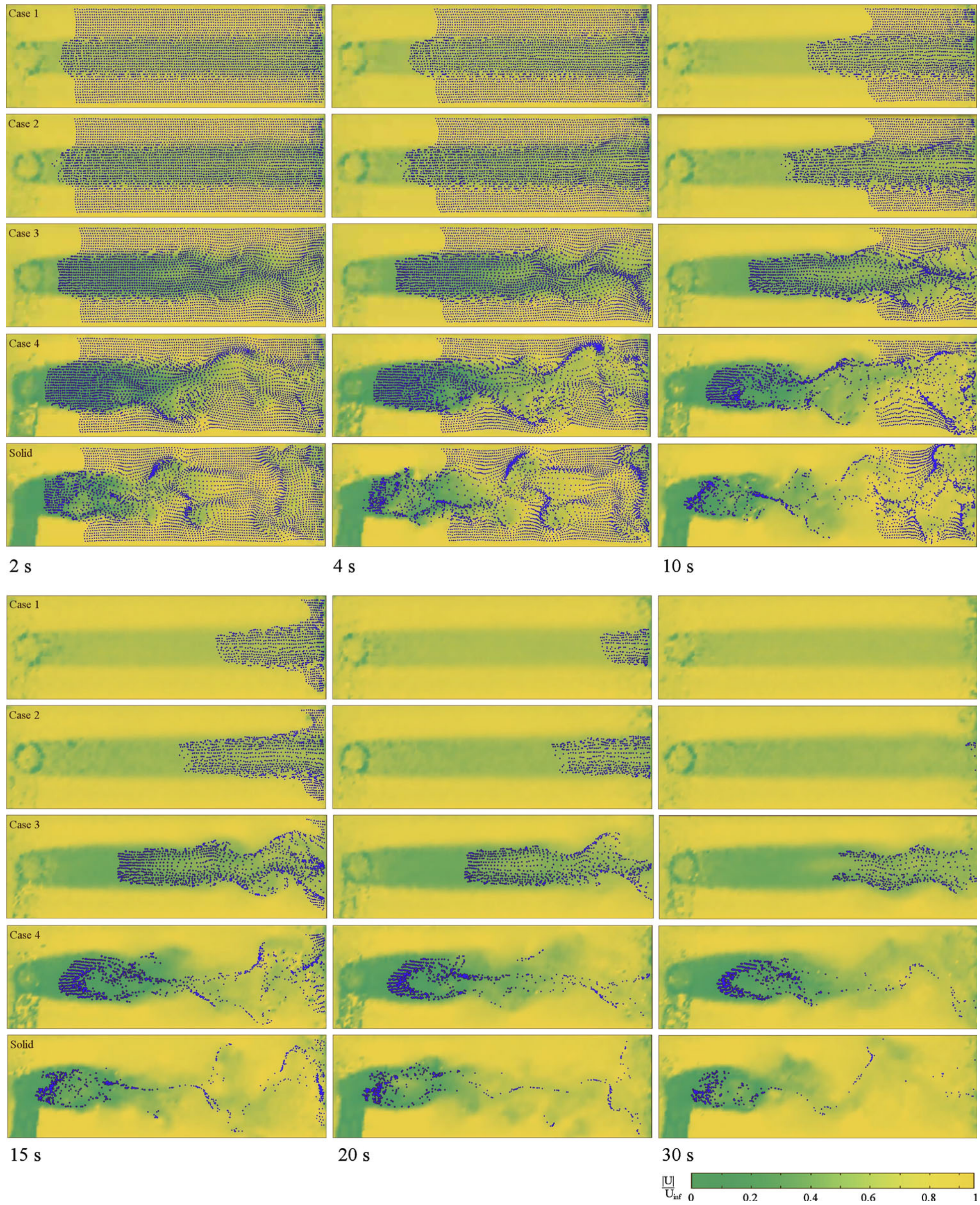

Fig. 6 Temporal dispersion of particles set in the wake of models of varying mesh void ($m = 8.89, 6.67, 4.45, 2.22$) and constant twine thickness ($t = 0.50$). Results for a solid cylinder are also presented for comparison

instability and mixing within the wake region as a result of the model's presence. Particle tracking allows to study dispersion motion, and it can be used to represent the behaviour of waste or nutrient particles in an aquaculture context. Dispersion rates behind and inside the model were calculated (Fig. 7). For the first flow regime, typified by Cases 1 and 2, the flow in the wake remains nearly laminar. The measured flow velocity in the wake is 65 % (Case 1) and 50 % (Case 2) of the upstream free flow. The wake can most readily be compared to a jet flow, where instabilities develop near regions of the flow with high-velocity gradients. This is consistent with our characterisation of the first flow regime, as essentially a penetrating flow, where streamlines pass through the model without any appreciable deformation.

In the second regime, as exemplified by Case 3, the streamwise velocity in the wake is reduced to 25 % of the free-stream velocity. Here instabilities develop, whereby large-scale oscillations in the wake are observed, evolving from a flapping motion into a vortex-dominated wake. As shown previously, this second flow regime is characterised by a partially penetrating flow, where streamlines still go through the model, but some are reoriented towards the outside of the model (the vertical y ordinate on the figures); in this case. the wake does not present a recirculation zone, but rather oscillates or generates vortex shedding.

The third regime is characterised by Case 4. Here, the flow in the wake is reduced to 1 % of the free-stream velocity at some locations, and the flow is similar to that past a solid cylinder. A fully developed recirculation zone is observed, exhibiting a von Kármán vortex street similar to that produced behind a solid cylinder. As a result of the reduced porosity, $\epsilon = 0.64$, the model behaves effectively like a solid cylinder with active blowing at the surface, resulting in vortex shedding and an increase in the vortex formation lengthscale (Fransson et al. 2004).

Particle dispersion shows that the first and second flow regimes advect the particles downstream relatively fast. For instance, for Case 2 (first flow regime), the velocity inside the wake is about $0.5\,U_{\mathrm{inf}}$ and there is very little turbulent mixing within the wake. In this case, the particles are advected in the wake at half the speed of the free-stream flow. However, for the third flow regime, the dispersion time is greatly increased. From Fig. 6, we observe that at times $t = 20$ s and $t = 30$ s a proportion of the particles are trapped inside a recirculation zone with a very slow velocity magnitude, $|U| \leq 0.02\,U_{\mathrm{inf}}$. Particles only escape this recirculation region through a slow diffusion process, which takes place where the shading is fully developed and vortices are dropped in the wake (for Case 4, at $x/D \geq 3.5D$).

To more precisely quantify particle dispersion, the percentage of particles still in field of view is plotted against time (Fig. 7a). The plots of dispersion rate behind the model show a similar trend for Cases 1, 2 and 5. These three models are classified as presenting the first flow regime. The reliance upon the diffusion mechanism for the escape of particles trapped within recirculation regions behind the models in the third flow regime (e.g. Case 4) is similar to that encountered with a solid cylinder; they show a similar logarithmic decay behind the obstacle. However, as the recirculation area is greater in the case of the porous models, the total dispersion time for a particle introduced at $t = 0$ is greater than for the solid cylinder (Fig. 7a).

Finally, the dispersion time is dependent on the parameter α; an increase in the parameter coincides with an increased dispersion time (Fig. 7a). This suggests that the dispersion is not only dependent on the averaged flow velocity in the wake, but also dependent on the twine/mesh ratio. This conjecture is reinforced by the fact that the models within the third flow regime all fall under this trend despite the fact that the flow velocity field does not collapse with the parameter α. Finally, we note that PIV data obtained with the 100-mm focal-length lens (not presented here), and analysed using a similar particle tracking approach, shows similar trends except for model Case 7. In this case, a faster decay rate is observed than for Case 6. The models within the first flow regime have the fastest dispersion rate, one which is nearly linear with a slope of -12. By contrast, the models within the third flow regime have a dispersion rate which becomes linear, after a first slower decay, with a slope coefficient of -9.

4 Conclusions

The main objective of this paper was to investigate the impact of the twine/mesh ratio on the flow through a short porous hollow cylinder inspired by aquaculture fish nets. The first results were obtained by flow visualisation using dye and are in agreement with similar investigations Zong and Nepf (2011), Gansel et al. (2012) despite using a lower Reynolds number. Three different flow regimes were observed: (1) a laminar regime where streamlines pass through the model without any visible disturbances, (2) a transitional regime where the wake of the partially penetrating flow creates a velocity gradient resulting in the formation of instabilities, akin to a Kelvin-Helmholtz instability, and (3) a fully developed recirculation zone exhibiting a von Kármán vortex street similar to that produced behind a solid cylinder. Varying the surface

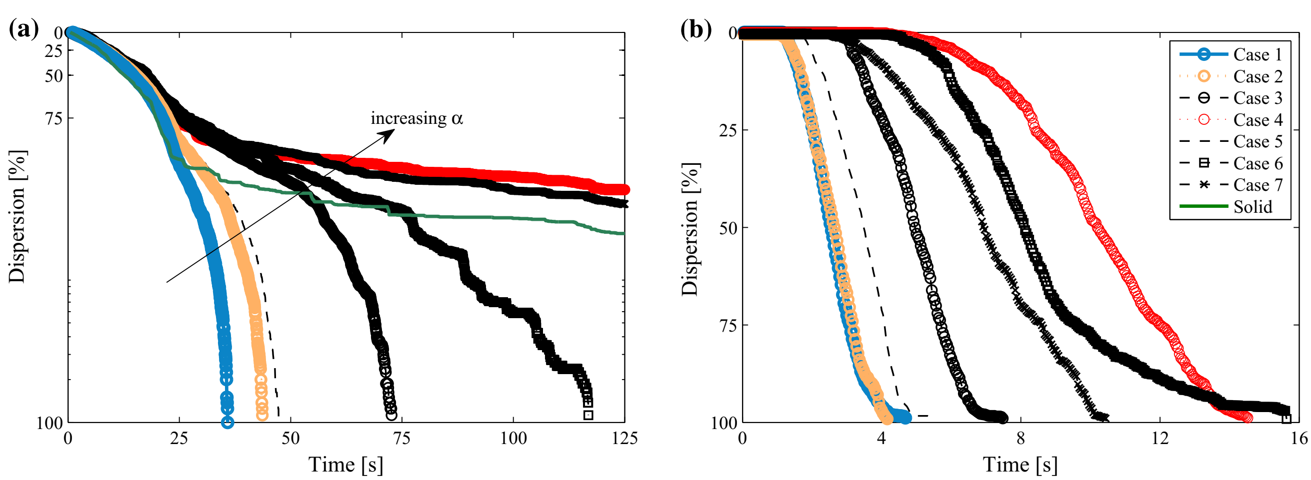

Fig. 7 **a** Dispersion rate of the particles behind the model ($x/L \in [0 : 10.25]$ and $y/l \in [-1.3 : 1.3]$) at time $t = 0$; **b** dispersion rate of the particles inside the model at time $t = 0$

geometry is sufficient to alter the flow from one regime to another without having to modify the inside porosity of the obstruction, unlike (Nicolle and Eames 2011; Zong and Nepf 2011).

These observations were further elucidated by PIV measurements and two-dimensional particle tracking on the resulting flow fields. This also gave access to the dispersion rate. The models belonging to the first flow regime group were seen to have the fastest dispersion rate, whereas those belonging to the third flow regime not only have the slowest dispersion rate, but also a logarithmic decay slower than that of the solid cylinder. At equivalent surface porosity, the bleed flow can vary from one model to another, resulting in a different dispersion rate.

The normalised velocities in the wake of each model were observed to have very different magnitudes, ranging from nearly 0 to 0.7 depending upon the flow regime. Models with the exact same surface porosity have a wake of different velocity magnitude (up to three time higher in some cases), and it does not appear to be possible to collapse these experimental data using ϵ alone. Therefore, we can conclude that the surface porosity factor ϵ is not the key parameter defining the flow topology. An empirical parameter α, based on the twine/mesh ratio and defined as $\alpha = t^{0.5}D^{0.5}/m$, has instead been identified as collapsing the data for the first and second flow regimes. At $Re = 800$, the transition to or from the third flow regime happens for a value of α between 1.23 and 1.42. It is not immediately clear why the aforementioned scaling is not applicable to the third regime. This regime represents twine dynamics that differs from the other two regimes. The individual twines no longer behave as an array of obstacles with independent wakes, but rather as a solid obstacle with a bleed flow. This variation in the local flow dynamics could be responsible for the failure of the scaling.

Our findings provide data on the dependence between the global flow dynamics, the bleed flow and the surface porosity of a bluff body. Future confirmation of our results for larger scale experiments, and therefore at higher Reynolds number, could help the aquaculture industry to optimise the twine/mesh ratio of future net production.

Acknowledgments This work was supported by a Faculty of Engineering Faculty Research Development Fund at the University of Auckland. We gratefully acknowledge the helpful and insightful comments of the referees.

References

Arcas DR, Redekopp LG (2004) Aspects of wake vortex control through base blowing/suction. Phys Fluids 16:452–456

Baek H, Karniadakis GE (2009) Suppressing vortex-induced vibrations via passive means. J Fluid Struct 25:848–866

Ball DJ, Stansby PK, Alliston N (1996) Modelling shallow water flow around pile groups. Proc Inst Civ Eng Wat Marit Energy 118:226236

Bhattacharyya S, Dhinakaran S, Khalili A (2006) Fluid motion around and through a porous cylinder. Chem Eng Sci 61:4451–4461

Billant P, Chomaz J, Huerre P (1998) Experimental study of vortex breakdown in swirling jets. J Fluid Mech 376:183–219

Buryniuk M, Petrell RJ, Baldwin S, Lo KV (2006) Accumulation and natural disintegration of solid wastes caught on a screen suspended below a fish farm cage. Aquac Eng 35:78–90

Camarri S, Fallenius BEG, Fransson JHM (2013) Stability analysis of experimental flow fields behind a porous cylinder for the investigation of the large-scale wake vortices. J Fluid Mech 715:499–536

Coutanceau M, Bouard R (1977) Experimental determination of the main features of the viscous flow in the wake of a circular cylinder in uniform translation. Part 1. Steady flow. J Fluid Mech 79:231–256

Delaunay Y, Kaiktsis L (2001) Control of circular cylinder wakes using base mass transpiration. Phys Fluids 13:3285

Dong S, Triantafyllou GS, Karniadakis GE (2008) Elimination of vortex streets in bluff-body flows. Phys Rev Lett 100:204501

FAO (2010) The state of world fisheries and aquaculture. Tech. rep., Food and Agriculture Organization of the United Nations

Feng LH, Wang JJ (2012) Synthetic jet control of separation in the flow over a circular cylinder. Exp Fluids 53:467–480

Fransson JHM, Konieczny P, Alfredsson PH (2004) Flow around a porous cylinder subject to continuous suction or blowing. J Fluid Struct 19:1031–1048

Gansel LC, McClimans TA, Myrhaug D (2012) Average flow inside and around fish cages with and without fouling in a uniform flow. J Offshore Mech Artic Eng 134:041201-1

Halwart M, Soto D, Arthur JR (2007) Cage aquaculture regional reviews and global overview. FAO Fisheries Technical Paper 498

Klebert P, Lader P, Gansel LC, Oppedal F (2013) Hydrodynamic interactions on net panel and aquaculture fish cages: a review. Ocean Eng 58:260–274

Kristiansen T, Faltinsen OM (2012) Modelling of current loads on aquaculture net cages. J Fluid Struct 34:218–235

Lader PF, Enerhaug B (2005) Experimental investigation of forces and geometry of a net cage in uniform flow. IEEE J Ocean Eng 30:79–84

Levy B, Liu YZ (2013) The effects of cactus inspired spines on the aerodynamics of a cylinder. J Fluid Struct 39:335–346

Mandal S, Datta N, Sahoo T (2013) Hydroelastic analysis of surface wave interaction with concentric porous and flexible cylinder systems. J Fluid Struct 42:437–455

Moe H, Fredheim A, Hopperstadt OS (2010) Structural analysis of aquaculture net cages in current. J Fluid Struct 26:503–516

Nicolle A, Eames I (2011) Numerical study of flow through and around a circular array of cylinders. J Fluid Mech 679:1–31

Norberg C (2003) Fluctuating lift on a circular cylinder: review and new measurements. J Fluid Struct 17:57–96

Ozkan GM, Oruc V, Akilli H, Sahin B (2013) Flow around a cylinder surrounded by a permeable cylinder in shallow water. Exp Fluids 53:1751–1763

Salama NKG, Murray AG (2011) Farm size as a factor in hydrodynamic transmission of pathogens in aquaculture fish production. Aquac Environ Interact 2:61–74

Sheard GJ, Leweke T, Thompson MC, Hourigan K (2007) Flow around an impulsively arrested circular cylinder. Phys Fluids 19:083601

Stickney R (2009) Aquaculture an introductory text. Cambridge University Press, Cambridge

Subasinghe R, Soto D, Jia J (2009) Global aquaculture and its role in sustainable development. Rev Aquac 1:2–9

Takemura T, Tanaka N (2007) Flow structures and drag characteristics of a colony-type emergent roughness model mounted on a flat plate in uniform flow. Fluid Dyn Res 39:694

Torrissen O, Jones S, Asche F, Guttormsen A, Skilbrei OT, Nilsen F, Horsberg TE, Jackson D (2013) Salmon lice impact on wild salmonids and salmon aquaculture. J Fish Dis 36:171–194

Venayagamoorthy SK, Ku H, Fringer OB, Chiu A, Naylor RL, Koseff JR (2011) Numerical modeling of aquaculture dissolved waste transport in a coastal embayment. Environ Fluid Mech 11:329–352

Williamson CHK (1996) Vortex dynamics in the cylinder wake. Annu Rev Fluid Mech 28:477–539

Williamson CHK, Roshko A (1988) Vortex formation in the wake of an oscillating cylinder. J Fluid Struct 2:355–381

Wood CJ (1967) Visualization of an incompressible wake with base bleed. J Fluid Mech 29:259–272

Zdravkovich MM (1981) Review and classification of various aerodynamic and hydrodynamic means for suppressing vortex shedding. J Wind Eng Ind Aerodyn 7:145–189

Zhao YP, Guib FK, Xua TJ, Chena XF, Cuic Y (2013) Numerical analysis of dynamic behavior of a box-shaped net cage in pure waves and current. Appl Ocean Res 35:158–167

Zhao YP, Li YC, Dong GH, Gui FK, Teng B (2007) Numerical simulation of the effects of structure size ratio and mesh type on three-dimensional deformation of the fishing-net gravity cage in current. Aquac Eng 36:285–301

Zong L, Nepf H (2011) Vortex development behind a finite porous obstruction in a channel. J Fluid Mech 691:368–391